Three-dimensional solitons in Rydberg-dressed Bose–Einstein condensates with spin–orbit coupling and a radially periodic potential

Dong Zhao [a,b,1], Qihong Huang [a,b,1], Shulei Gao [a,c], Hongyan Yang [a,c], Di Wu [a,c], Boris A. Malomed [d,e] , Li Xue [a,b,*], Siliu Xu [a,c] ,*

[a] *Key Laboratory of Optoelectronic Sensing and Intelligent Control, Hubei University of Science and Technology, Xianning, 437100, China*
[b] *School of Electronic and Information Engineering, Hubei University of Science and Technology, Xianning, 437100, China*
[c] *School of Biomedical Engineering and Imaging, Xianning Medical College, Hubei University of Science and Technology, Xianning 437100, China*
[d] *Department of Physical Electronics, School of Electrical Engineering, Faculty of Engineering, Tel Aviv University, P.O.B. 39040, Ramat Aviv, Tel Aviv, Israel*
[e] *Instituto de Alta Investigación, Universidad de Tarapacá, Casilla 7D, Arica, Chile*

ARTICLE INFO

ABSTRACT

We propose a model of three-dimensional (3D) Rydberg-dressed spinor (two-component) Bose–Einstein condensates (BECs), with the spin–orbit coupling (SOC) and an axisymmetric radially periodic potential. It produces various species of stable 3D solitons with different vorticities in its two components. The shape and stability of the soliton are determined by the system's control parameters: the SOC strength (λ), coefficients of the contact and Rydberg–Rydberg interactions (σ and U_{ij}, respectively), and the depth (w_0) of the radial potential. The ground-state 3D solitons, with the lowest set of topological charges in its components, one of which is 0 and the other one is ± 1 (these states are known as semivortices), keep the axial symmetry. Excited states with higher topological charges, which are unstable in previously studied SOC systems, feature broken axial symmetry, but may be dynamically stable states. In the absence of SOC, we also find stable two-component solitons with crescent- and hollow-shaped components.

1. Introduction

The study of nonlinear wave phenomena in atomic Bose–Einstein condensates (BECs) has garnered considerable attention in recent years [1–5]. Depending on the sign of the interatomic interactions, BECs can exhibit the formation of bright or dark solitons. Properties of these solitons are critically affected by the spatial dimension of the condensate. Specifically, multidimensional states in BECs with attractive interactions may be susceptible to the collapse, whereas those with repulsive interactions may be prone to snaking instabilities [6,7]. Therefore, the creation of three-dimensional (3D) bright solitons poses a greater challenge compared to the generation of their one-dimensional (1D) and two-dimensional (2D) counterparts [8]. In particular, while 1D solitons can be produced by integrable equations, this is not feasible for 2D and 3D solitons. Another fundamental problem is the instability driven by the possibility of the collapse in the 3D case with the attractive nonlinearity.

Several scenarios have been proposed for stabilization of 3D solitons, such as the use of materials exhibiting saturable or competing nonlinearities [9–11], nonlocality of the nonlinearity [12–14], special types of nonlinear interactions [15,16], optical tandem schemes [17, 18], waveguide arrays and optical lattices inscribed in waveguides [19–21], as well the use of the spin–orbit coupling (SOC) in binary BECs [22, 23]. Recently, the Rydberg electromagnetically-induced-transparency (Rydberg-EIT) system has been proposed as a promising platform for generating stable 3D solitons [24,25]. In the latter case, cold atomic gases provide effective media for the creation, propagation, and storage of ultraslow fundamental solitons and vortices [26–29].

The introduction of optical lattices into nonlinear media can significantly enhance the stability of localized wave structures in BEC [19–21,30–32]. Typically, optical lattices are induced by interference of counter-propagating laser beams [33,34]. By applying optical lattices to BEC, experiments have successfully produced bright gap solitons [35] and truncated gap waves [36] in 1D space. Predictions have also been made for the existence of 2D gap solitons and vortical solitons in pancake/disk-shaped BECs trapped by 2D optical-lattice potentials [37,38]. Furthermore, 3D Weyl solitons [39], gap solitons, and vortices have been predicted in spherical [40,41] and dipolar [42] BEC, loaded into 3D optical lattices. Both 2D and 3D gap and vortical solitons can be

---

stabilized as well by low-dimensional optical lattices [19,20,43–45]. The possibility of the existence of stable multidimensional soliton-like states, supported by 2D and 3D periodic optical-lattice potentials and described by the density-functional model, has been extended to superfluid Fermi gases [46,47]. Notably, recent applications of 2D parity-time symmetric potentials [48–51] and moiré lattices [52,53] have also demonstrated their efficacy in stabilizing various solitons.

SOC BECs, which have been realized experimentally [54,55], have also drawn much interest. These systems not only facilitate the study of phenomena associated with artificial vector gauge potentials [56], but also give rise to numerous remarkable structures [57,58]. SOC notably alters the dispersion relation of the system [59–61], breaks the Galilean invariance [62,63], significantly affects properties of 1D solitons [64,65] and creates stable multi-dimensional ones [66–68]. Of particular interest is the effect of SOC on BECs in the presence of external potentials, in which case the potential's symmetry determines possible symmetries of self-trapped solitons and their evolution [69–71].

In spite of the recent progress, the understanding of 3D matter-wave solitons in binary condensates, sustained by the interplay of SOC and Rydberg–Rydberg interactions (RRI) in the presence of a radially periodic potential, was not developed. The present study aims to systematically construct 3D stable solitons in this system by means of numerical analysis. These are various stable self-sustained states, featuring axisymmetric zero-vorticity and vorticity-carrying modes with different topological charges in its two spinor components. It is found that the ground-state solitons keep the axial symmetry. On the other hand, excited states exhibit broken axial symmetry. These observations underscore the profound impact of SOC and Rydberg–Rydberg interactions on the structure and stability of the solitons. In the absence of SOC, a novel species of stable 3D solitons, crescent- and hollow-shaped ones, have been found.

The following contents are structured as follows: the model and formulations are proposed in Section 2, results of the systematic investigation of the 3D matter-wave solitons are reported in Section 3, and the paper is concluded by Section 4.

2. The model

We consider a three-level cold atomic system which is shown in Fig. 1(a). States $|g\rangle$ and $|n'p\rangle$ are the ground and excited states of the cold atoms, while $|e\rangle \equiv |ns\rangle$ is the excited Rydberg state with principal quantum number n. The transitions $|g\rangle \rightarrow |n'p\rangle$ and $|n'p\rangle \rightarrow |e\rangle$ are driven by the laser fields with Rabi frequency Ω_1 and Ω_2, and detuning Δ_1 and Δ_2, respectively. The system reduces to an effective two-level one under condition $\Delta_1 \gg \Omega_1$ [72]. Then, the effective Rabi frequency and detuning are $\Omega = (\Omega_1 \Omega_2)/2\Delta_1$ and $\Delta = \Delta_1 + \Delta_2$, respectively, as shown in Fig. 1(b).

The long-range interaction between different Rydberg atoms is modeled by the van der Waals potential $V_{vdW} = \hbar V(\mathbf{r}' - \mathbf{r})$, where

$$V(\mathbf{r}' - \mathbf{r}) = C_6 \left[R_b^6 + |\mathbf{r}' - \mathbf{r}|^6 \right], \tag{1}$$

$C_6 < 0$ is the dispersion parameter, $\mathbf{r}$ and $\mathbf{r}'$ are position vectors of the interacting atoms, with coordinates $\mathbf{r} = (X, Y, Z)$. Further, $\hbar$ is the Planck's constant and $R_b = \left[|C_6 \Delta| / |\Omega|^2 \right]^{1/6}$ is the Rydberg blockade radius [72].

In the mean-field approximation, the dynamics of 3D BECs is governed by the system of Gross–Pitaevskii equations (GPEs) for the two components of the spinor wave function, $\psi = (\psi_+, \psi_-)$, with the

Rashba-type SOC:

$$i\hbar \frac{\partial \Psi_+}{\partial T} = \left[-\frac{\hbar^2}{2M} \nabla^2_{X,Y,Z} - \hat{V}_{SO+} - W(\rho) - \left(g|\Psi_+|^2 + g|\Psi_-|^2 \right) \right.$$
$$\left. - \int d^3\mathbf{R}' \left(V_{11} |\Psi_+|^2 + V_{12} |\Psi_-|^2 \right) \right] \Psi_+,$$
$$i\hbar \frac{\partial \Psi_-}{\partial T} = \left[-\frac{\hbar}{2M} \nabla^2_{X,Y,Z} - \hat{V}_{SO-} - W(\rho) - \left(g|\Psi_+|^2 + g|\Psi_-|^2 \right) \right.$$
$$\left. - \int d^3\mathbf{R}' \left(V_{21} |\Psi_+|^2 + V_{22} |\Psi_-|^2 \right) \right] \Psi_-. \tag{2}$$

Here the atomic kinetic energy is represented by the Laplacian, $\nabla^2_{X,Y,Z} = \partial^2/\partial X^2 + \partial^2/\partial Y^2 + \partial^2/\partial Z^2$, T is time, M is the atomic mass, and coefficient $g = 4\pi\hbar^2 a/M$ accounts for the contact interaction between atoms, with the s-wave scattering length a. It may be assumed equal for intra- and inter-species collisions between atoms which is usually adopted as a good approximation in the numerical simulations, and the two species (components) represents two different hyperfine states of the same atom [73,74]. The Rashba-type SOC operators are defined as

$$\hat{V}_{SO+}\Psi_+ = i\Lambda \left(\frac{\partial \Psi_-}{\partial X} - i\frac{\partial \Psi_-}{\partial Y} + \frac{\partial \Psi_+}{\partial Z} \right),$$
$$\hat{V}_{SO-}\Psi_- = i\Lambda \left(\frac{\partial \Psi_+}{\partial X} + i\frac{\partial \Psi_+}{\partial Y} - \frac{\partial \Psi_-}{\partial Z} \right), \tag{3}$$

where Λ is the SOC coefficient [75]. The external potential W is adopted here as one which is periodic with respect to the radial coordinate, $\rho \equiv \sqrt{X^2 + Y^2}$, in the (X, Y) plane, viz., $W(\rho) = 2V_0 \cos^2(\rho/\rho_0)$, with modulation depth V_0 and radial period $\pi\rho_0$ [45,76]. The last terms in Eq. (2) represent the potential of the long-range interaction between Rydberg atoms, $V_{ij}(\mathbf{r}' - \mathbf{r}) = C_6^{ij} \left[R_b^6 + |\mathbf{r}' - \mathbf{r}|^6 \right]$ [cf. Eq. (1)], with van der Waals coefficients C_6^{ij} $(i, j = 1, 2)$, which are subject to the symmetry constraint, $C_6^{12} = C_6^{21}$. Thus, only V_{11}, V_{12} and V_{22} are considered in the following discussions.

The spatial coordinates, time, and wave functions are rescaled as $\mathbf{r} \equiv (x, y, z) = (X, Y, Z)/R_b$, $t = t/\tau$, with the temporal scale $\tau = MR_b^2/\hbar$, and $\psi_{1,2} = R_b^{3/2} N^{-1/2} \Psi_{1,2}$, with the total norm (number of atoms) $N = N_+ + N_- \equiv \iiint \left[|\psi_+|^2 + |\psi_-|^2 \right] d^3\mathbf{r}$. Accordingly, the GPE system (2) is cast in the dimensionless form:

$$i\frac{\partial \psi_+}{\partial t} = \left[-\frac{1}{2}\nabla^2_{x,y,z} - V_{SO+} - w(r) - \sigma\left(|\psi_+|^2 + |\psi_-|^2 \right) \right.$$
$$\left. - \int d^3\mathbf{r}' \left(u_{11} |\psi_+|^2 + u_{12} |\psi_-|^2 \right) \right] \psi_+,$$
$$i\frac{\partial \psi_-}{\partial t} = \left[-\frac{1}{2}\nabla^2_{x,y,z} - V_{SO-} - w(r) - \sigma\left(|\psi_+|^2 + |\psi_-|^2 \right) \right.$$
$$\left. - \int d^3\mathbf{r}' \left(u_{21} |\psi_+|^2 + u_{22} |\psi_-|^2 \right) \right] \psi_-, \tag{4}$$

where $\nabla^2_{x,y,z} = \partial^2/\partial x^2 + \partial^2/\partial y^2 + \partial^2/\partial z^2$, $r = \sqrt{x^2 + y^2} \equiv \rho/R_b$, the rescaled axisymmetric potential is

$$w(r) = 2w_0 \cos^2(r/r_0), \, w_0 \equiv V_0 \left(MR_b/\hbar \right)^2, \, r_0 \equiv \rho_0/R_b, \tag{5}$$

the rescaled SOC coefficient is $\lambda \equiv MR_b\hbar^{-2}\Lambda$. Further, the rescaled coefficient of the contact interaction is $\sigma \equiv gNM\left(R_b^4/\hbar \right)$, and the RRI potential is

$$u_{ij}(\mathbf{r}' - \mathbf{r}) = \frac{U_{ij}}{1 + (\mathbf{r} - \mathbf{r}')^6}, \, U_{ij} \equiv \frac{MNC_6^{(ij)}}{\hbar^2 R_b^4}. \tag{6}$$

Numerical results are reported below, chiefly, for $r_0 = 1$ in potential (5). Systems with $r_0 \neq 1$ yield results similar to those reported here for $r_0 = 1$. This choice implies that the period of the radial potential is close to the radius of the Rydberg blockade, which is the subject of main interest in the present work, as it makes it possible to study new effects, produced by the interplay of the radially periodic potential and RRI. Another parameter regime, in which the potential's period is much larger than the blockade radius (i.e., RRI is much stronger), is
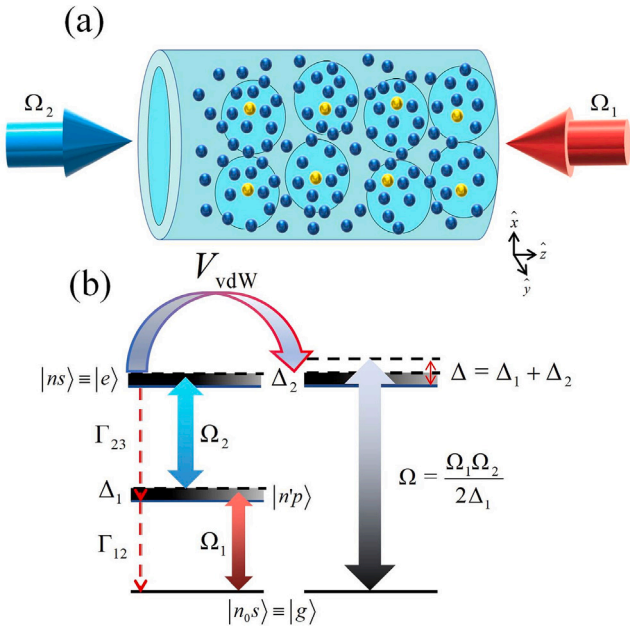
Fig. 1. (a) The schematic of the Rydberg-dressed Bose–Einstein condensates system. Yellow and blue balls represent the Rydberg and normal atoms, respectively. (b) Energy levels of the Rydberg atoms.

Table 1
Parameters of the 3D matter-wave solitons with the corresponding topological charges.

(m_+, m_-)	σ	λ	w_0	U_{11}	U_{12}	U_{22}	N
(0, 1)	1	1.3	5	1	1	1	1
(1, 2)	0.3	1	3.5	1	1	1	1
(2, 3)	0.3	2	3.5	1	1	1	1
(3, 4)	1	0.1	1.5	1	1	1	1
(−1, 0)	0.3	1	3.5	1	1	1	1
(−2, −1)	0.3	1	3.5	1	1	1	1
(−3, −2)	0.3	3	3	1	1	1	1

similar to the previously studied situation in the free space, which gives rise to characteristic features of the bosonic condensates with long-range atomic interactions, such as the roton minimum in the underlying spectrum [77].

Characteristic values of the corresponding physical parameters may be taken as those for the ultracold gas of ^{88}Sr atoms, which is available for the experimental realization [28]. In this case, the RRI coefficients are $C_6 = 2\pi \times 81.6$ GHz μm^6, $R_b = 10$ μm, and the temporal scale is $\tau = 0.18$ s.

The energy of this system is expressed as [78,79]

$$E_{\text{tot}} = \int (\varepsilon_{\text{k}} + \varepsilon_{\text{SOC}} + \varepsilon_{\text{contact}} + \varepsilon_{\text{RRI}} + \varepsilon_{\text{ext}}) \mathrm{d}^3 r$$

$$\varepsilon_{\text{k}} = \frac{1}{2} \left(|\nabla \psi_+|^2 + |\nabla \psi_-|^2 \right)$$

$$\varepsilon_{\text{SOC}} = -\frac{i\lambda}{2} \left[\psi_+^* \left(\frac{\partial \psi_-}{\partial x} - i \frac{\partial \psi_-}{\partial y} + \frac{\partial \psi_+}{\partial z} \right) \right.$$
$$\left. + \psi_-^* \left(\frac{\partial \psi_+}{\partial x} + i \frac{\partial \psi_+}{\partial y} - \frac{\partial \psi_-}{\partial z} \right) \right] + \text{c.c.}$$

$$\varepsilon_{\text{contact}} = -\frac{1}{2} \sigma \left(|\psi_+|^4 + |\psi_-|^4 + 2|\psi_+|^2 |\psi_-|^2 \right) \tag{7}$$

$$\varepsilon_{\text{RRI}} = -\frac{1}{2} |\psi_+|^2 \int \mathrm{d}^3 r' \left(u_{11} |\psi_+|^2 + u_{12} |\psi_-|^2 \right)$$
$$- \frac{1}{2} |\psi_-|^2 \int \mathrm{d}^3 r' \left(u_{21} |\psi_+|^2 + u_{22} |\psi_-|^2 \right)$$

$$\varepsilon_{\text{ext}} = -\frac{1}{2} w(r) \left(|\psi_+|^2 + |\psi_-|^2 \right),$$

where ε_k, ε_{SOC}, $\varepsilon_{\text{contact}}$, ε_{RRI}, and ε_{ext} represent the kinetic, SOC, contact, RRI, and external potential energies, respectively. Here, c.c. represent the complex conjugate.

3. The results

Stationary solutions to Eq. (4) are sought for in the usual form, $\psi_\pm = \phi_\pm e^{-i\mu t}$, where μ is the chemical potential, and $\phi_\pm$ are components of the stationary wave function. In the cylindric coordinates (ρ, θ, z), the initial ansatz for the 3D system is chosen as [80]

$$\phi_\pm = A_\pm \left(\rho^2 + z^2 \right)^{|m_\pm|/2} \exp \left[-\left(\rho^2 + z^2 \right) + i m_\pm \theta \right], \tag{8}$$

where $m_- = m_+ + 1$ is the usual relation between the integer vorticities (topological charges) of the two components, which is compatible with Eq. (4) [66], and $A_\pm$ are their initial amplitudes. In particular, the states with topological charge 0 in one component, and $|m_\pm| = 1$ in the other are categorized as *semivortices* (SVs) [22,66]. It is relevant to stress that the normal form of a vortex component in the 3D space should include factor $\rho^{|m_\pm|}$, rather than $\left(\rho^2 + z^2 \right)^{|m_\pm|/2}$ in the input (8). In the course of simulations, the shape of the solitons quickly rearranges itself into the one with the "correct" radial factor, $\rho^{|m_\pm|}$.

As the solitons in the SOC system carry orbital angular momentum (OAM), it is necessary to define the corresponding characteristics of the solitons. Following Ref. [79], we define normalized OAM values of the two components and the total one as, respectively,

$$\left\langle L_\pm \right\rangle = \int \frac{\psi_\pm^* \hat{L} \psi_\pm}{N_\pm} \mathrm{d}^3 r,$$
$$\left\langle L \right\rangle = \frac{N_+ \left\langle L_+ \right\rangle + N_- \left\langle L_- \right\rangle}{N_+ + N_-}, \tag{9}$$

where $\hat{L} = -i(x \partial/\partial y - y \partial/\partial x)$ is the OAM operator.

We have obtained stable 3D solitons by means of the imaginary-time integration method [81], applied to Eq. (4). The time derivative in Eq. (4) is taken as $i \partial \psi_\pm / \partial t = \mu \psi_\pm$, and the second derivations of $\phi_\pm$ with respect to coordinates are dealt with the discrete Fourier transformations $\phi_\pm(r) = \mathcal{F}^{-1}[(ik)^2]\mathcal{F}(\phi_\pm(r))$, where $\mathcal{F}$ and $\mathcal{F}^{-1}$ represent the discrete Fourier and inverse Fourier transformations, and k is the wavenumber. Typical examples of the stable solitons with $m_+ \geq 0$ and $m_\pm \leq 0$ are shown in Figs. 2 and 3, respectively. It is observed that, for the SV modes, with $(m_+, m_-) = (0, 1)$ or $(-1, 0)$), the density distribution is axisymmetric, with nonzero and zero values of the amplitude at the central point ($\rho = 0$) in the fundamental and vortex components, respectively, the latter one being patterned as a ring. The phase-circulation pattern in the semi-vortex is axisymmetric too.

On the other hand, in Figs. 2(b-d,f-h) and 3(b,c,e,f), the annular solitons with both components carrying nonzero vorticity (they were called excited states in Ref. [66]) demonstrate broken axial symmetry, This feature is explained by azimuthal instability of axisymmetric ring-shaped modes, which is similar to the generic property of 2D SOC solitons with nonzero vorticity in both components [66]. The number of fragments produced by the instability is equal to the value of the respective topological charges. The vortex solitons with $m_\pm < 0$ being less vulnerable to the axial-symmetry breaking than ones with $m_\pm > 0$, due to the fact the SOC operators (3) correspond to a particular sign of the underlying twist.

We stress that all the solitons displayed in Figs. 2 and 3, including the ones with broken axial symmetry, represent stationary states produced by the imaginary-time simulations, and they all are *stable* if used as initial conditions for simulations of the perturbed real-time evolution, in the framework of Eq. (4). This result is drastically different from that reported for the simple 2D SOC system in Ref. [66], where all the excited states were found to be unstable.

To present the results in the systematic form, Fig. 4(a) produces the energy-band spectrum of the linearized version of Eq. (4). The spectrum demonstrates the semi-infinite bandgap and two finite ones, that may host soliton families as solutions of the full nonlinear system.
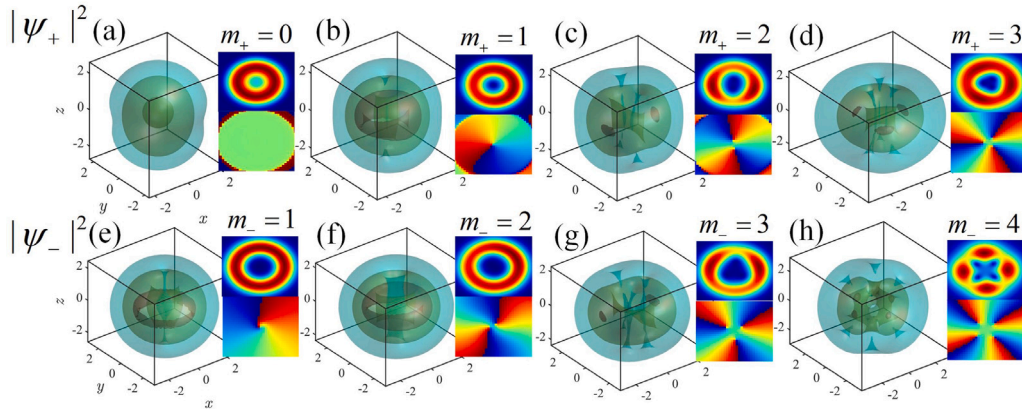
Fig. 2. 3D vortex matter-wave solitons with topological charges of their components $(m_+, m_-) = (0, 1), (1, 2), (2, 3), (3, 4)$. Insets display the density distribution and phase structure in the (x, y) plane. Parameters of the system are shown in Table 1. Three density iso-surfaces are plotted with density cuts $0.96|\psi_\pm|^2_{max}$, $0.4|\psi_\pm|^2_{max}$, $0.04|\psi_\pm|^2_{max}$ for the 3D matter-wave solitons. This is also adopted for the other iso-surface figures in this paper.
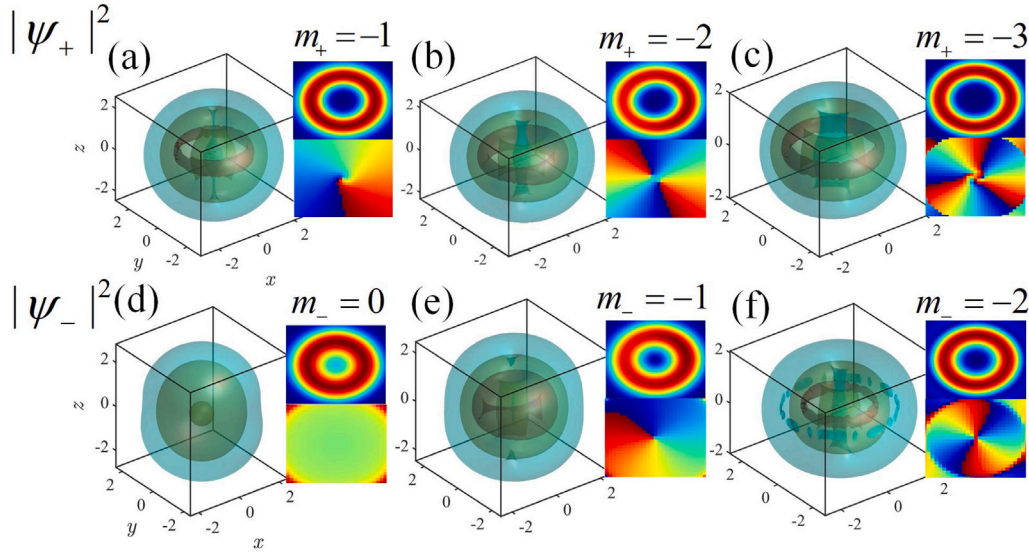

Fig. 3. The same as in Fig. 2, but for the 3D vortex matter-wave solitons with the components' topological charges $(m_+, m_-) = (-1, 0), (-2, -1), (-3, -2)$.

In particular, point A in the figure corresponds to the 3D soliton with parameters

$$(m_+, m_-, \lambda, \sigma, w_0, U_{11}, U_{12}, U_{22}) = (0, 1, 1.3, 1, 5, 1, 1, 1). \quad (10)$$

The variations of parameters for the 3D solitons in Fig. 4(b-f) are all based on point A.

In particular, the relation between chemical potential μ and norm N is presented in Fig. 4(b). Naturally, it is found that the ground state, characterized by $(m_+, m_-) = (0, 1)$, exhibits the lowest chemical potential. As the topological charge m increases, the chemical potential of the system gradually rises. The variation of μ with the norm is nearly negligible, i.e., the soliton family forms a nearly-flatband family, cf. Ref. [82].

The effect of the SO coupling coefficient, λ, on the norm is presented in Fig. 4(c), featuring the natural symmetry around $\lambda = 0$. The range of λ varies significantly depending on the topological charge: (i) For $m_+ = 0$ and 1, the range of λ is continuous, and stable solutions persist even at $\lambda \to 0$. (ii) When $m_+ = 2$, the ranges of λ are separated by a gap which is denoted by the dashed lines in Fig. 4(c), indicating that the SOC effect is crucial for the stabilization of the solitons with higher topological charges.

The norm as a function of the contact-interaction coefficient σ and nonlocal RRI strengths U_{11} and U_{12} are plotted in Figs. 4(d,e,f). It is seen

that the ground-state 3D solitons, with $(m_+, m_-) = (0, 1)$, consistently exhibits the lowest norm. Note that the local interaction coefficient σ may take both positive and negative values, and, at $\sigma \to 0$, there is a notable increase in the norm of the vortex soliton with higher topological charges, $(m_+, m_-) = (2, 3)$, as seen in Fig. 4(d). The RRI coefficients U_{11} and U_{12} may also be positive or negative. When U_{11} or U_{12} take specific values, such as $U_{11} = 3$ or $U_{12} = 3$, there is a significant increase in the norm for vortex solitons with higher topological charges, as demonstrated in Figs. 4(e) and (f).

The stability of these 3D solitons was tested by the simulations of the perturbed evolution, performed in the framework of Eq. (4), using the fourth-order Runge–Kutta algorithm. Fig. 5 displays an example of the evolution of the vortex soliton with topological charges $(m_+, m_-) = (1, 2)$. In this case, the spatial and phase patterns of the evolving soliton stay virtually intact, up to $t = 1000$ (at least), exhibiting its full stability.

The stability domains in (N, λ), (N, σ), (N, U_{11}) and (N, U_{12}) planes, as identified by the systematic simulations, are displayed in Fig. 6, where the topological charges are $(m_+, m_-) = (1, 2)$, with other parameters in each panels fixed as per Table 1. It is found that the SOC strength λ in the stability area may take both positive and negative values, in ranges of $(0.6 \sim 2.7)$ and $(-2.7 \sim -0.6)$, respectively, exhibiting symmetry with respect to $\lambda = 0$, as seen in Fig. 6 (a). This finding agrees with that reported above in Fig. 4(c). For the parameters fixed in
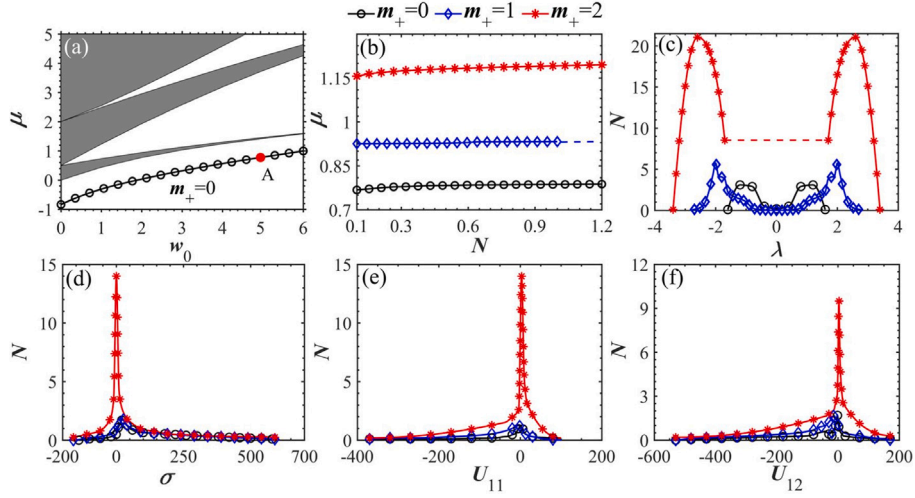
Fig. 4. (a) The band spectrum of the linear system with parameters $(m_+, m_-, \lambda, \sigma, U_{11}, U_{12}, U_{22}) = (0, 1, 1.3, 0, 0, 0, 0)$. The black circles in panel (a) indicate the $\mu(w_0)$ relation when the nonlinearity is taken into consideration, where $(\sigma, U_{11}, U_{12}, U_{22}) = (1, 1, 1, 1)$, and the norm is fixed as $N = 1$. (b) Chemical potential μ vs norm N. (c-f) The norm as a function of parameters λ, σ, U_{11}, and U_{12}. The black, blue and red lines represent the solitons with topological charges $m_+ = 0, 1$, and 2, respectively. Solid and dashed segments corresponds to stable and unstable 3D solitons, respectively. The variation of the parameters in panels (b-f) corresponds to point A in panel (a), with the parameters given by (Eq. (10)).
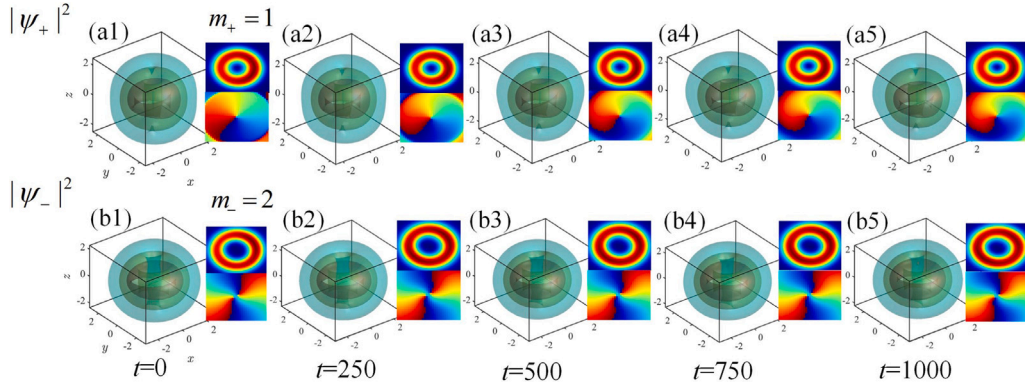

Fig. 5. The simulated evolution of the vortex soliton with topological charges $(m_+, m_-) = (1, 2)$. The top and bottom rows display the evolution of ψ_+ and ψ_- components, respectively.

Table 1, norm N takes values in the green stability domain in each panel of Fig. 6. Note that all stability domains exhibit a single-peak shape. Notably, the contact-interaction strength σ, as well as in RRI strengths, U_{11} and U_{12}, may be both positive and negative in the stability domain, albeit it is larger for $U_{11,12} < 0$. While $U_{22} = 1$ is fixed in each panel, further analysis has shown that the stability domain corresponding to the variation of U_{22} is similar to those corresponding to U_{11} and U_{12}.

The stability domain in the (λ, w_0) plane is shown in Fig. 7. As we mentioned above, this domain is symmetric for regions $\lambda > 0$ and $\lambda < 0$, therefore only the stability domain with $\lambda > 0$ is displayed in Fig. 7(a).

The phase of the 3D solitons in the (x, y) plane features a multi-layer structure in the radial direction, with the number of layers represented by integer number n (alias the radial quantum number). Note that n increases with the increase of λ, as shown in Figs. 7(b-e). For example, for fixed $w_0 = 0.5$, the soliton has two layers ($n = 2$) where $\lambda = 1.4$ [Fig. 7(b)], while we get $n = 4, 6, 8$ for $\lambda = 2.5, 3.5, 4.6$, respectively, see Fig. 7(c,d,e). In fact, this structure of the 3D solitons implies that, if SOC is strong enough, it gives rise to the solitons created on top of the spatially modulated multi-layer background. The stability domains of solitons with different numbers of the phase layers are designated by different colors in Fig. 7(a). Stable solitons do not exist in two regions which are painted gray where the soliton solutions are hard to obtain or cannot last long time in these parametric regions.

The energy of 3D solitons, calculated as per Eq. (7), is plotted in Fig. 8(a), which shows that the total energy increases practically linearly as the function of norm N, the ground state with topological charges $(m_+, m_-) = (0, 1)$ having the lowest energy. The normalized OAM, calculated pursuant to Eq. (9), is displayed, as a function of topological charge m_+ and norm N, in Figs. 8(b,c,d). The normalized OAM of the ψ_+ component is equal to $|m_+|$, i.e., $\langle L_+ \rangle = |m_+|$, as shown in Fig. 8(b). Similarly, we get $\langle L_- \rangle = |m_-| = |m_+ + 1|$. The normalized OAM of the 3D solitons is independent of the norm, suggesting the conservation of the system's OAM, as illustrated in Figs. 8(c,d).

In the absence of SOC ($\lambda = 0$), the calculations produce crescent- and hollow-shaped two-component solitons, corresponding to topological charges $(m_+, m_-) = (-1, 0)$, as shown in Fig. 9. For the ψ_+ component with $m_+ = -1$, one observes that the cross section of these 3D solitons in the (x, y) plane exhibits a crescent-like profile. The phase distribution of this component displays vortex characteristics, where the phase circulates clockwise around a pivot, which is not centered in the (x, y) plane. In contrast, the ψ_- component (with topological charge $m_- = 0$) exhibits a plain phase structure. The evolution of this crescent-hollow-shaped two-component soliton shows that its spatial and phase distributions remain nearly unchanged, at least, up to $t = 2000$, as seen in Figs. 9(a5,b5).

To investigate the energy current caused by the topological charge (vorticity), we studied the effect of the internal transverse current, which is defined as $\vec{S}_\pm = \frac{i}{2} (\psi_\pm \nabla \psi_\pm^* - \psi_\pm^* \nabla \psi_\pm)$, on the stability of
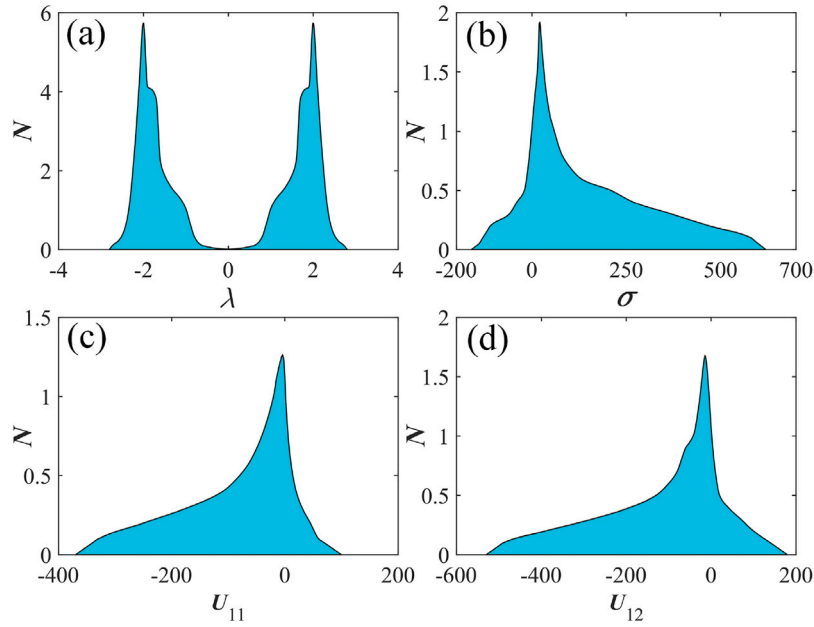
Fig. 6. Stability domains for norm N of the vortex solitons with $(m_+, m_-) = (1, 2)$, corresponding to the variation of parameters λ, σ, U_{11}, and U_{12}. Stable and unstable zones are painted green and white, respectively. The other system parameters in each panels are fixed as $\sigma = 0.3$, $\lambda = 1$, $w_0 = 3.5$, and $U_{11} = U_{12} = U_{22} = 1$.
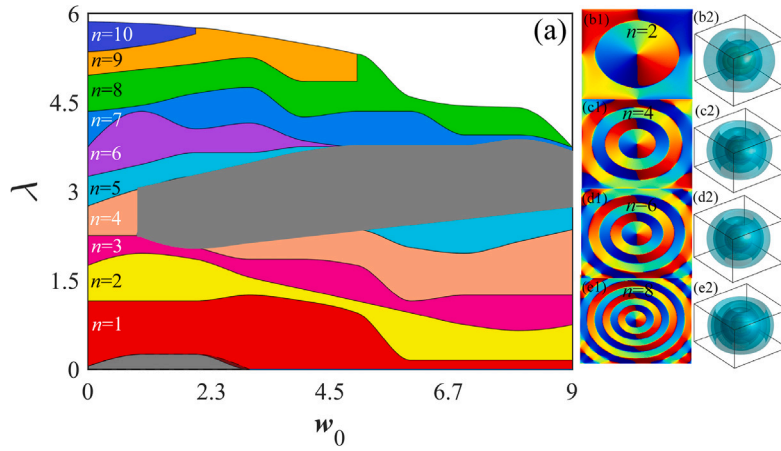

Fig. 7. Stability domains of the vortex solitons with topological charges $(m_+, m_-) = (-1, 0)$, displayed in the (λ, w_0) plane. (a) Integer n stands for the number of the radial layers in the phase structure, which are also designated by different colors. Stable solitons do not exist in white and gray regions. (b,c,d,e) The phase structures and norm distributions with the numbers of radial layers $n = 2, 4, 6, 8$, the corresponding values of SOC strength λ being $1.4, 2.5, 3.5$, and 4.6, respectively. The system's parameters are $\sigma = 0.3$ and $U_{11} = U_{12} = U_{22} = 0.1$.

matter-wave solitons in the 3D system (4) [83]. In this connection, Fig. 10 displays the internal current $\vec{S}_+$ and $\vec{S}_-$ for the two components of the 3D soliton with topological charges $(m_+, m_-) = (-1, 0)$. In the ψ_+ component, the internal current displays a crescent-like distribution, matching the norm distributions in the (x, y) and (x, z) planes. The direction of the internal current, as shown by black arrows in Fig. 10(a), is determined by the respective topological charge ($m_+ = -1$). The results indicate that the internal OAM results in the energy current in the vortex matter-wave solitons. On the other hand, for the ψ_- component, with topological charge $m_- = 0$, the internal current is negligible, with an amplitude $S_- \sim 10^{-22}$, as shown in Fig. 10(b), while the amplitude of S_+ is $\sim 10^{-6}$.

4. Conclusion

In this study, we have explored the dynamics of 3D Rydberg-dressed two-component matter-wave solitons, under the action of SOC between

the components, in the combination with the axisymmetric radially periodic potential. Employing the imaginary-time integration method, we have produced stable 3D solitons. The ground-state solitons, with the lowest topological charges $(0, +1)$ and $(-1, 0)$ in the two components, keep the axial symmetry. On the other hand, excited states, with higher values of the topological charges, which are known to be unstable in previously studied SOC models, exhibit broken axial symmetry, while remaining stable in the real-time simulations. These observations underscore the profound impact of SOC and Rydberg–Rydberg interactions on the structure and stability of the solitons.

All identified solitons, including those with broken symmetry, are dynamically stable under real-time evolution simulations. The stability domain accommodates both positive and negative SOC strengths, contact-interaction strengths, and Rydberg–Rydberg interaction strengths. The radial phase structure of 3D solitons exhibits multi-layer patterns, characterized by the radial quantum number, suggesting that strong SOC can influence solitons on spatially modulated backgrounds.
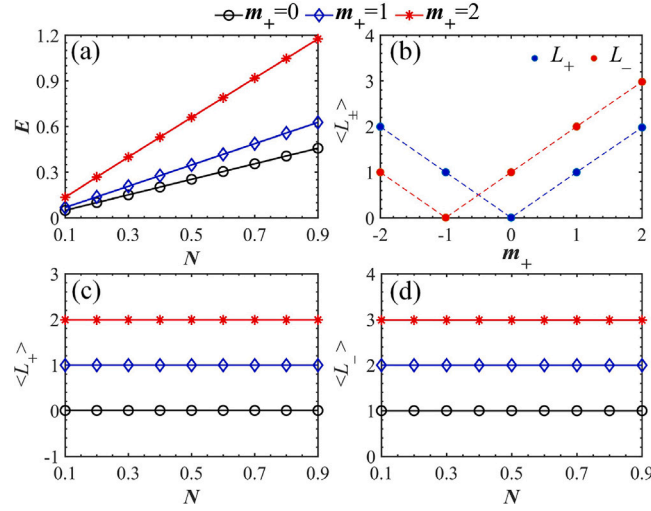
Fig. 8. (a) The total energy of the 3D solitons vs. norm N. (b) The normalized orbital angular momentum $\langle L_\pm \rangle$ vs. topological charge m. (c,d) Two components of the normalized OAM $\langle L_+ \rangle$ and $\langle L_- \rangle$ as function of norm N. The system's parameters are the same as in Table 1.
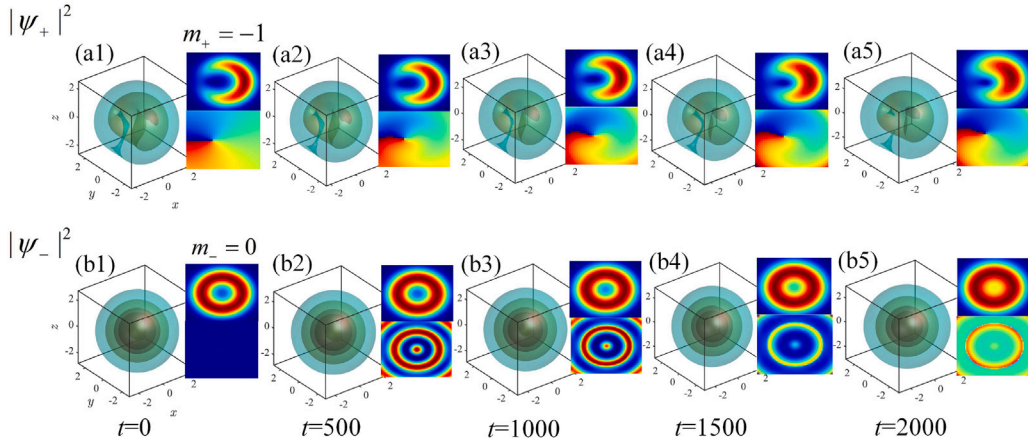

Fig. 9. The evolution of a 3D soliton with the topological charge $(m_+, m_-) = (-1, 0)$, which features the crescent-like and hollow shapes of its components. Insets display the intensity distribution and phase structure in the (x, y) plane. The system's parameters are $\sigma = -1$, $\lambda = 0$, $w_0 = 5$, $N = 0.5$, $U_{11} = U_{12} = U_{22} = 1$.
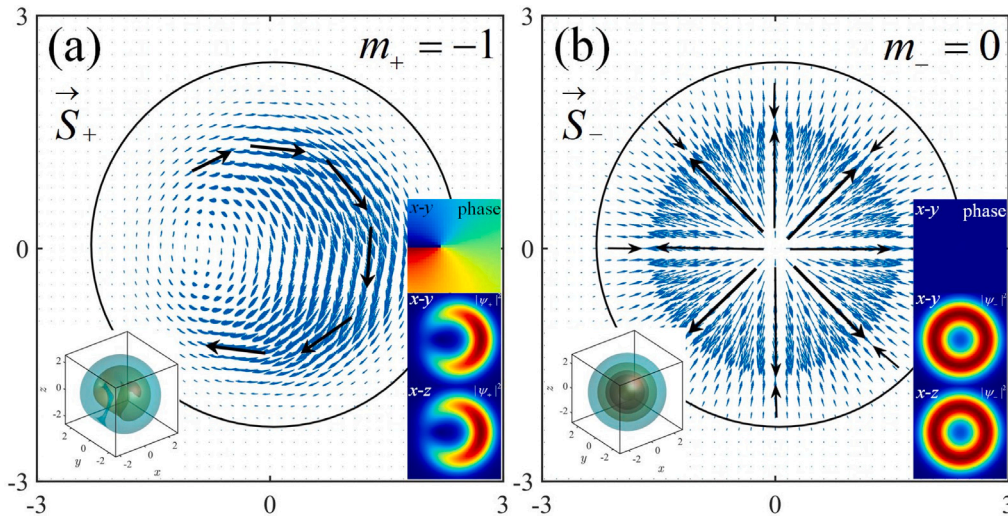

Fig. 10. The internal current of the crescent-shaped (a) and hollow (b) components of the 3D soliton, with topological charge $(m_+, m_-) = (-1, 0)$. The insets display 3D profiles, phase structure in the (x, y) plane, and intensity distributions in the (x, y) and (x, z) planes. Black arrows represent the local direction of the internal current. The system's parameters are the same as in Fig. 9.

In the absence of SOC, the numerical results have revealed a novel species of stable 3D solitons with two components, crescent- and hollow-shaped ones. These findings not only expand the understanding of the complex interplay between SOC, contact interactions, and Rydberg dressing in spinor BEC, but also suggest new possibilities for exploring exotic quantum states and phenomena in related systems. By carefully modulating physical parameters in the similar experiment setup [84–89], our structures in this paper are expected to be found.

CRediT authorship contribution statement

Dong Zhao: Conceptualization. **Qihong Huang:** Software, Investigation. **Shulei Gao:** Visualization, Investigation. **Hongyan Yang:** Investigation. **Di Wu:** Methodology. **Boris A. Malomed:** Writing – original draft. **Li Xue:** Writing – original draft, Resources. **Siliu Xu:** Writing – review & editing, Funding acquisition.

Declaration of competing interest

The authors declare that they have no known competing financial interests or personal relationships that could have appeared to influence the work reported in this paper.

Acknowledgments

Data availability

Numerical data generated for the research described in the article is available on a reasonable request.

References

[1] Pethick C, Smith H. Bose–Einstein condensation in dilute gases. England: Cambridge University Press; 2002.

[2] Kevrekidis PG, Frantzeskakis DJ, Carretero-González R. Emergent nonlinear phenomena in Bose–Einstein condensates: theory and experiment. New York: Springer; 2008.

[3] Fetter AL. Rotating trapped Bose–Einstein condensates. Rev Modern Phys 2009;81:647.

[4] Malomed BA. Multidimensional soliton systems. Adv Phys: X 2024;9:2301592.

[5] Mihalache D. Localized structures in optical media and Bose–Einstein condensates: An overview of recent theoretical and experimental results. Rom Rep Phys 2024;76:402.

[6] Bergé L. Wave collapse in physics: principles and applications to light and plasma waves. Phys Rep 1998;303:259.

[7] Kuznetsov EA, Dias F. Bifurcations of solitons and their stability. Phys Rep 2011;507:43.

[8] Malomed BA. Multidimensioanl solitons. Melville, NY: AIP Publishing; 2022.

[9] Desyatnikov A, Maimistov A, Malomed B. Three-dimensional spinning solitons in dispersive media with the cubic-quintic nonlinearity. Phys Rev E 2000;61:3107.

[10] Mihalache D, Mazilu D, Crasovan LC, Towers I, Buryak AV, Malomed BA, Torner L, Torres JP, Lederer F. Stable spinning optical solitons in three dimensions. Phys Rev Lett 2002;88:073902.

[11] Liang G, Zhang H, Fang L, Shou Q, Hu W, Guo Q. Influence of transverse cross-phases on propagations of optical beams in linear and nonlinear regimes. Laser & Photonics Rev 2020;14:2000141.

[12] Maucher F, Henkel N, Saffman M, likowski WKró, Skupin S, Pohl T. Rydberg-induced solitons: three-dimensional self-trapping of matter waves. Phys Rev Lett 2011;106:170401.

[13] Tikhonenkov I, Malomed BA, Vardi A. Anisotropic solitons in dipolar Bose–Einstein condensates. Phys Rev Lett 2008;100:090406.

[14] Zhang H, Zhou T, Dai C. Stabilization of higher-order vortex solitons by means of nonlocal nonlinearity. Phys Rev A 2022;105:013520.

[15] Kartashov YV, Malomed BA, Torner L. Solitons in nonlinear lattices. Rev Modern Phys 2011;83:247.

[16] Falcão-Filho EL, de Araújo CB, Boudebs G, Leblond H, Skarka V. Robust two-dimensional spatial solitons in liquid carbon disulfide. Phys Rev Lett 2013;110:013901.

[17] Torner L, Carrasco S, Torres JP, Crasovan LC, Mihalache D. Tandem light bullets. Opt Commun 2001;199:277.

[18] Torner L, Kartashov YV. Light bullets in optical tandems. Opt Lett 2009;34:1129.

[19] Baizakov BB, Malomed BA, Salerno M. Multidimensional solitons in a low-dimensional periodic potential. Phys Rev A 2004;70:053613.

[20] Mihalache D, Mazilu D, Lederer F, Kartashov YV, Crasovan L-C, Torner L. Stable three-dimensional spatiotemporal solitons in a two-dimensional photonic lattice. Phys Rev E 2004;70:055603.

[21] Mihalache D, Mazilu D, Lederer F, Malomed BA, Kartashov YV, Crasovan L-C, Torner L. Stable spatiotemporal solitons in Bessel optical lattices. Phys Rev Lett 2005;95:023902.

[22] Zhang YC, Zhou ZW, Malomed BA, Pu H. Stable solitons in three dimensional free space without the ground state: self-trapped Bose–Einstein condensates with spin–orbit coupling. Phys Rev Lett 2015;115:253902.

[23] Li H, Xu SL, Belić MR, Cheng JX. Three-dimensional solitons in Bose–Einstein condensates with spin–orbit coupling and Bessel optical lattices. Phys Rev A 2018;98:033827.

[24] Chen MW, Hu HJ, Zhu M, Zhou QQ, Qiu ZC, Li BB, Zhao Y, Xue L, Xu SL. Weak-light solitons and their active control in Rydberg-dressed parity-time symmetry Moiré optical lattices. Results Phys 2023;48:106392.

[25] Liao QY, Hu HJ, Chen MW. Two-dimensional spatial solitons in optical lattices with Rydberg-Rydberg interaction. Acta Phys Sin 2023;72:104202.

[26] Zhao Y, Lei YB, Xu YX, Xu SL, Triki H, Biswas A, Zhou Q. Vector spatiotemporal solitons and their memory features in cold Rydberg gases. Chin Phys Lett 2022;39:034202.

[27] Guo YW, Xu SL, He JR, Deng P, Belić MR, Zhao Y. Transient optical response of cold Rydberg atoms with electromagnetically induced transparency. Phys Rev A 2020;101:023806.

[28] Bai Z, Li W, Huang G. Stable single light bullets and vortices and their active control in cold Rydberg gases. Optica 2019;6:309.

[29] Liao B, Li S, Huang C, Luo Z, Pang W, Tan H, Malomed BA, Li Y. Anisotropic semivortices in dipolar spinor condensates controlled by Zeeman splitting. Phys Rev A 2017;96:043613.

[30] Abo-Shaeer JR, Raman C, Vogels JM, Ketterle W. Observation of vortex lattices in Bose–Einstein condensates. Science 2001;292:476.

[31] Mandel O, Greiner M, Widera A, Rom T, Hänsch TW, Bloch I. Controlled collisions for multi-particle entanglement of optically trapped atoms. Nature 2003;425:937.

[32] Wang Q, Mihalache D, Belić MR, Zeng L, Lin J. Spiraling Laguerre-Gaussian solitons and arrays in parabolic potential wells. Opt Lett 2023;48:4233–6.

[33] Chin C, Grimm R, Julienne P, Tiesinga E. Feshbach resonances in ultracold gases. Rev Modern Phys 2010;82:1225.

[34] Kengne E, Liu WM, Malomed BA. Spatiotemporal engineering of matter-wave solitons in Bose–Einstein condensates. Phys Rep 2021;899:1.

[35] Eiermann B, Th Anker, Albiez M, Taglieber M, Treutlein P, Marzlin KP, Oberthaler MK. Bright Bose–Einstein gap solitons of atoms with repulsive interaction. Phys Rev Lett 2004;92:230401.

[36] Th Anker, Albiez M, Gati R, Hunsmann S, Eiermann B, Trombettoni A, Oberthaler MK. Nonlinear self-trapping of matter waves in periodic potentials. Phys Rev Lett 2005;94:020403.

[37] Ostrovskaya EA, Kivshar YS. Matter-wave gap solitons in atomic band-gap structures. Phys Rev Lett 2003;90:160407.

[38] Sakaguchi H, Malomed BA. Dynamics of positive- and negative-mass solitons in optical lattices and inverted traps. J Phys B 2004;37:1443–59.

[39] Shang C, Zheng Y, Malomed BA. Weyl solitons in three-dimensional optical lattices. Phys Rev A 2018;97:043602.

[40] Mihalache D, Mazilu D, Lederer F, Malomed BA, Crasovan LC, Kartashov YV, Torner L. Stable three-dimensional solitons in attractive Bose–Einstein condensates loaded in an optical lattice. Phys Rev A 2005;72. 021601(R).

[41] Alexander TJ, Ostrovskaya EA, Sukhorukov AA, Kivshar YS. Three-dimensional matter-wave vortices in optical lattices. Phys Rev A 2005;72:043603.

[42] Muruganandam P, Adhikari, SK. Gap solitons in a dipolar Bose–Einstein condensate on a three-dimensional optical lattice. J Phys B 2011;44:121001.

[43] Luz HLFDa, Abdullaev FK, Gammal A, Salerno M, Tomio L. Matter-wave two-dimensional solitons in crossed linear and nonlinear optical lattices. Phys Rev A 2010;82:043618.

[44] Abdullaev FK, Gammal A, Luz HLFDa, Salerno M, Tomio L. Three-dimensional solitons in cross-combined linear and nonlinear optical lattices. J Phys B 2012;45:115302.

[45] Kartashov YV, Zezyulin DA. Stable multiring and rotating solitons in two-dimensional spin–orbit-coupled Bose–Einstein condensates with a radially periodic potential. Phys Rev Lett 2019;122:123201.

[46] Xue JK, Zhang AX. Superfluid Fermi gas in optical lattices: self-trapping, stable, moving solitons and breathers. Phys Rev Lett 2008;101:180401.

D. Zhao et al.

Chaos, Solitons and Fractals: the interdisciplinary journal of Nonlinear Science, and Nonequilibrium and Complex Phenomena 196 (2025) 116416

[47] Adhikari SK, Malomed BA. Gap solitons in a model of a superfluid fermion gas in optical lattices. Phys D 2009;238:1402.

[48] Li GM, Li A, Su SJ, Zhao Y, Huang KY, Zhou GP, Xue L, Xu SL. Vector spatiotemporal solitons in cold atomic gases with linear and nonlinear $\mathcal{PT}$ symmetric potentials. Opts Express 2021;29:14016.

[49] Suchkov SV, Sukhorukov AA, Huang J, Dmitriev SV, Lee C, Kivshar YS. Nonlinear switching and solitons in PT-symmetric photonic systems. Laser Photonics Rev 2016;10:77.

[50] Xu SL, Li H, Zhou Q, Zhou GP, Zhao D, Belić MR, He JR, Zhao Y. Parity-time symmetry light bullets in a cold Rydberg atomic gas. Opt Express 2020;28:16322–32.

[51] Kartashov YV, Hang C, Huang G, Torner L. Three-dimensional topological solitons in PT-symmetric optical lattices. Optica 2016;3:1048.

[52] Wang P, Zheng Y, Chen X, Huang C, Kartashov YV, Torner L, Konotop VV, Ye F. Localization and delocalization of light in photonic Moiré lattices. Nature 2020;577:422.

[53] Li BB, Zhao Y, Xu SL, Zhou Q, Fu QD, Ye FW, Hua CB, Chen MW, Hu HJ, Zhou QQ. Two-dimensional gap solitons in parity-time symmetry Moiré optical lattices with Rydberg-Rydberg interaction. Chin Phys Lett 2023;40:044201.

[54] Lin YJ, Jiménez-García K, Spielman IB. Spin–orbit-coupled Bose–Einstein condensates. Nature 2011;471:83.

[55] Chisholm CS, Hirthe S, Makhalov VB, Ramos R, Vatr'e R, Cabedo J, Celi A, Tarruell L. Probing supersolidity through excitations in a spin–orbit-coupled Bose–Einstein condensate. 2024, arXiv:2412.13861.

[56] Colloquium: Artificial gauge potentials for neutral atoms. Rev Modern Phys 2011;83:1523.

[57] Xu XQ, Han JH. Spin–orbit coupled Bose–Einstein condensate under rotation. Phys Rev Lett 2011;107:200401.

[58] Xu Y, Zhang Y, Wu B. Bright solitons in spin–orbit-coupled Bose–Einstein condensates. Phys Rev A 2013;87:013614.

[59] Wang C, Gao C, Jian CM, Zhai H. Spin–orbit coupled spinor Bose–Einstein condensates. Phys Rev Lett 2010;105:160403.

[60] Sinha S, Nath R, Santos L. Trapped two-dimensional condensates with synthetic spin–orbit coupling. Phys Rev Lett 2011;107:270401.

[61] Zhang Y, Mao, Zhang C. Mean-field dynamics of spin–orbit coupled Bose–Einstein condensates. Phys Rev Lett 2012;108:035302.

[62] Zhu Q, Zhang C, Wu B. Exotic superfluidity in spin–orbit coupled Bose–Einstein condensates. Europhys Lett 2012;100:50003.

[63] Hamner C, Zhang Y, Khamehchi MA, Davis MJ, Engels P. Spin–orbit-coupled Bose–Einstein condensates in a one-dimensional optical lattice. Phys Rev Lett 2015;114:070401.

[64] Achilleos V, Frantzeskakis DJ, Kevrekidis PG, Pelinovsky DE. Matter-wave bright solitons in spin–orbit coupled Bose–Einstein condensates. Phys Rev Lett 2013;110:264101.

[65] Kartashov YV, Konotop VV, Zezyulin DA. Bose–Einstein condensates with localized spin–orbit coupling: Soliton complexes and spinor dynamics. Phys Rev A 2014;90:063621.

[66] Sakaguchi H, Li B, Malomed BA. Creation of two-dimensional composite solitons in spin–orbit-coupled self-attractive Bose–Einstein condensates in free space. Phys Rev E 2014;89:032920.

[67] Zhang YC, Zhou ZW, Malomed BA, Pu H. Stable solitons in three-dimensional free space without the ground state: Self-trapped Bose–Einstein condensates with spin–orbit coupling. Phys Rev Lett 2015;115:253902.

[68] Jiang X, Fan Z, Chen Z, Pang W, Li Y, Malomed BA. Two-dimensional solitons in dipolar Bose–Einstein condensates with spin–orbit coupling. Phys Rev A 2016;93:023633.

[69] Xu SL, Lei YB, Du JT, Zhao Y, Hua R, Zeng JH. Three-dimensional quantum droplets in spin–orbit-coupled Bose–Einstein condensates. Chaos Solitons Fractals 2022;164:112665.

[70] Kartashov YV, Konotop VV, Abdullaev FKh. Gap solitons in a spin–orbit-coupled Bose–Einstein condensate. Phys Rev Lett 2013;111:060402.

[71] Zhang Y, Xu Y, Busch T. Gap solitons in spin–orbit-coupled Bose–Einstein condensates in optical lattices. Phys Rev A 2015;91:043629.

[72] Henkel N, Nath R, Pohl T. Three-dimensional roton excitations and super-solid formation in Rydberg-excited Bose–Einstein condensates. Phys Rev Lett 2010;104:195302.

[73] Galitski V, Spielman IB. Spin–orbit coupling in quantum gases. Nature 2013;494:49.

[74] Stanescu TD, Anderson B, Galitski V. Spin–orbit coupled Bose–Einstein condensates. Phys Rev A 2008;78:023616.

[75] Bindel JR, Pezzotta M, Ulrich J, Liebmann M, Sherman EY, Morgenstern M. Probing variations of the Rashba spin–orbit coupling at the nanometre scale. Nat Phys 2016;12:920–5.

[76] Baizakov B, Malomed BA, Salerno M. Matter-wave solitons in radially periodic potentials. Phys Rev E 2006;74:066615.

[77] Astrakharchik GE, Boronat J, Kurbakov IL, Lozovik YE. Quantum phase transition in a two-dimensional system of dipoles. Phys Rev Lett 2007;98:060405.

[78] Huang C, Ye Y, Liu S, He H, Pang W, Malomed BA, Li Y. Excited states of two-dimensional solitons supported by spin–orbit coupling and field-induced dipole–dipole repulsion. Phys Rev A 2018;97:013636.

[79] Zhao Y, Huang Q, Gong T, Xu S, Li Z, Malomed BA. Three-dimensional solitons supported by the spin–orbit coupling and Rydberg-Rydberg interactions in PT-symmetric potentials. Chaos Solitons Fractals 2024;187:115329.

[80] Chen XW, Deng ZG, Xu XX, Li SL, Fan ZW, Chen ZP, Liu B, Li Y. Nonlinear modes in spatially confined spin–orbit-coupled Bose–Einstein condensates with repulsive nonlinearity. Nonlinear Dynam 2020;101:569–79.

[81] Yang J, Lakoba TI. Accelerated imaginary-time evolution methods for the computation of solitary waves. Stud Appl Math 2008;120:265–92.

[82] Fu QD, Wang P, Huang CM, Kartashov YV, Torner L, Konotop VV, Ye FW. Optical soliton formation controlled by angle twisting in photonic moire lattices. Nat Photonics 2020;41:663–8.

[83] Dong L, Huang C. Vortex solitons in fractional systems with partially parity-time-symmetric azimuthal potentials. Nonlinear Dynam 2019;98:1019.

[84] Si ZZ, Wang DL, Zhu BW, Ju ZT, Wang XP, Liu W, Malomed BA, Wang YY, Dai CQ. Deep learning for dynamic modeling and coded information storage of vector-soliton pulsations in mode-locked fiber lasers. Laser & Photon Rev 2024;18:2400097.

[85] Si ZZ, Ju ZT, Ren LF, Wang XP, Malomed BA, Dai CQ. Polarization-induced buildup and switching mechanisms for soliton molecules composed of noise-like-pulse transition states. Laser & Photon Rev 2025;19:2401019.

[86] Ju ZT, Si ZZ, Ren LF, Feng HY, Yan X, Zhang JH, Liu W, Dai CQ. Energy disturbance-induced collision between soliton molecules and switch dynamics in fiber lasers: periodic collision, oscillation, and annihilation. Opt Lett 2025;50:1321–4.

[87] Si ZZ, Ren LF, Wang DL, Ju ZT, Wang XP, Wang YY, Liu W, Dai CQ. Generation and π-phase-induced oscillations of multi-soliton molecular complexes in ultrafast fiber lasers based on MOF-253@Au. Chem Eng J 2025;505:159024.

[88] Fang Y, Han HB, Bo WB, Liu W, Wang BH, Wang YY, Dai CQ. Deep neural network for modeling soliton dynamics in the mode-locked laser. Opt Lett 2023;48:779–82.

[89] Si ZZ, Wang YY, Dai CQ. Switching, explosion, and chaos of multi-wavelength soliton states in ultrafast fiber lasers. Sci China Phys Mech Astron 2024;67:274211.